Microstructural characteristic of the 24Cr2SiMn super ferritic stainless steel synthesized using local Indonesian materials

Mohammad Dani [a], Arbi Dimyati [a], Parikin [a], Fadli Rohman [b, c], Riza Iskandar [c], Aziz Khan Jahja [a], Andon Insani [a], Syahbuddin [d], Ching An Huang [e]

[a] *Center for Science and Technology of Advanced Materials. BATAN Kawasan Puspiptek Serpong, Tangerang 15314, Indonesia*
[b] *Centre for Physics, Indonesian Institute of Sciences, LIPI, Kawasan Puspiptek Serpong, Tangerang, 15314, Indonesia*
[c] *Central Facility for Electron Microscopy (GFE), RWTH Aachen, Ahornstrasse 55, D-52074-Aachen, Germany*
[d] *Department of Mechanical Engineering, Faculty of Engineering, Pancasila University, Srengseng Sawah, Jagakarsa, Jakarta 12640 Indonesia*
[e] *Department of Mechanical Engineering, Chang Gung University, Taoyuan, Taiwan*

* *Corresponding author: ademulyawan@batan.go.id*

Abstract

Precipitation is a key factor for the mechanical properties of material at high temperature application. It is important to study the formation and stability of precipitates in order to optimize the material properties. In this article, the author presents the preliminary results of the microstructure including precipitates formation in Fe-24Cr-2Si-0.8Mn (wt%) super ferritic stainless steel. Both the X-ray and the HRPD neutron diffraction pattern characterizations showed the first four characteristic reflections intensity with Miller indices corresponding to the (110), (200), (211), (220) diffraction planes that are typical for diffracting plan (*hkl*) of bcc system. The Scanning Transmission Electron Microscopy (STEM)-High Angle Angular Dark Field (HAADF) images and semi-quantitative Energy-Dispersive X-ray Spectroscopy (EDS) revealed the presence of chromium-carbide and chromium rich precipitates in rod-like shape with the size of about 700 nm in length and 250 nm in width. EDX semi-quantification results showed that the precipitate in the ferritic sample typically consists of 55.04 wt%C, 0.78 wt%Si, 35.42 wt%Cr, 0.68 wt%Mn, and 8.37 wt%Fe. Moreover, Selected Area Electron Diffraction (SAED) analysis revealed $(Fe,Cr)_7C_3$ as one of the chromium-carbide formed as precipitates. Finally, HRTEM images showed atomic structure of matrix and precipitates at dendrite boundaries at atomic level.

Keywords: Super ferritic stainless steel, precipitates, XRD, HRPD, SEM, TEM

INTRODUCTION

It is known that raw materials for steel production is sufficiently available in Indonesia. Therefore, efforts are underway to design newer version of both austenitic and ferritic steels with different non-standard composition, utilizing the mining materials from domestic supply and at the same time reducing Indonesia dependency upon imported steels. It is expected that these non-standard steels will meet Indonesian industrial development requirements. One industrial sector that urgently needs newer and better designed steel materials is the energy sector, or more precisely the nuclear energy sector. Presently, efforts have been going on at Indonesia Nuclear Energy Agency (BATAN) to design and synthesize both the austenitic and ferritic type of future stainless steels used for high-temperature applications.

Currently, the author has been effectively and successfully engaged in the synthesis of a new ferritic-type alloy by powder metallurgy method. Within this framework, the author has designed and prepared a ferritic steel with a special composition, the Fe-24Cr-2Si-0.8Mn (wt%) super ferritic stainless steel (24Cr2SiMn SFSS). As an alternative method, new non-standard ferritic alloys with predetermined elemental composition have been synthesized using the powder metallurgy method. Previously, bulky Fe-24Cr-2Si-0.8Mn ferritic steel bars has been synthesized using the electromagnetic furnace at TELIMEK-LIPI, Bandung (Effendi et al., 2014) and its

magnetic properties has been investigated. Later on, the same ferritic steel with the same composition was synthesized using the powder metallurgy method (Dani et al., 2017) and its defects and precipitations formation were investigated.

In this report, the super ferritic stainless steel of Fe-24Cr-2Si-0.8Mn (wt%) samples were prepared to support of the nuclear power plant materials research activity, especially research involving the high-pressure heat-exchanger materials. However, in considering of the material composition, it has been attempted to use ferritic stainless steel as a heat exchanger 'blade' component material that requires high hardness, form stability, and high temperature corrosion resistance. Precipitation formed in materials is a key factor that dominates the mechanical properties of materials to be applied at high temperatures. Therefore, microstructures including precipitations in inter-dendrites to optimize material properties were investigated in this study.

EXPERIMENTAL

Materials

The Super Ferritic Stainless Steel (SFSS) containing of Fe-Cr-Si-Mn-Ni powder was melted at temperature of about 1400°C for 2 hours in an arc melting furnace. The SFSS was cooled inside the furnace until room temperature. Using an Optical Emission Spectroscopy (OES), the constituent of SFSS were determined and listed in Table 1.

Table 1. Chemical composition of Fe-24Cr-2Si-0.8Mn Super Ferritic Stainless Steel as a result of spark Optical Emission Spectroscopy (OES).

Element	Fe	Cr	Mn	Si	C	Ni
wt %	Balance	23,710	0,821	2,020	0,258	0,120

Element	Al	Ti	P	S
wt %	0,007	0,006	0,023	0,015

The unit cell structure was characterized using the PANalytical Empyrean X-ray diffractometer with Cu-target (λ = 1.5405 Å) and the HRPD neutron diffractometer DN2 with a wavelength λ of 1.8221 Å. Both diffractometers were installed in BATAN Serpong Nuclear facility. SEM analysis was performed by using SEM JSM 6510 LA from JEOL company, equipped with EDS detector from Jeol company.

More detailed analyses were performed by means of Transmission Electron Microscopy (TEM). The TEM samples were prepared via conventional technique by following procedure: cutting, grinding, 3 mm-disc cutting, polishing, dimpling, and final ion beam milling of the specimen using Gatan Duo Mill 600 DIF at 5 kV of accelerating voltage, 3 mA of beam current and maximal 18° of milling angle. TEM observations were carried out by using the TEM FEI Tecnai G2 F20 instrument, a field emission TEM operated at an accelerating voltage of 200 kV. It is equipped with EDAX energy dispersive X-Ray (EDX) detector, a Fischione high-angle angular dark field (HAADF) detector, and Gatan GIF 2000 Energy-Filter TEM (EFTEM).

The Difftools plugin (Mitchell et al., 2008) installed on Digital Micrograph™ and Java Electron Microscopy Software (JEMS) simulation software (Stadelmann, 2012) were used to analyze Electron diffraction patterns. The Digital Micrograph™ software was also used to process high-resolution TEM images. The EDX spectrum was replot using Microcal™ Origin®Software (OriginLab, 1999). All images were compiled using CorelDraw™ software.

RESULTS AND DISCUSSION

Elemental Composition

The chemical composition of SFSS results obtained from the Optical Emission Spectrometer (OES) test are presented in Table 1. The SFSS mainly composed of Cr (23.710 wt%), Si (2.020 wt%), Mn (0.821 wt%), and C (0.258 wt%). This composition demonstrates that this steel can be classified as the new Fe-24Cr-2Si-0.8Mn Super Ferritic Stainless Steel. Other elements were also detected in low content which were Ni, S, P, Al, and Ti.

Crystal Structure
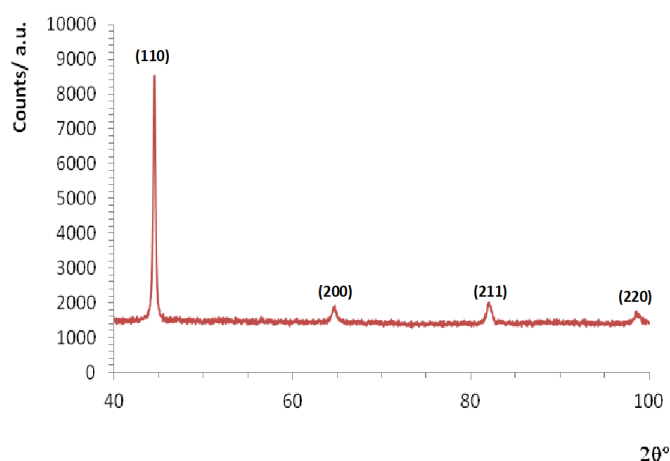
Fig. 1. X-ray Diffraction Intensity of Fe-24Cr-2Si-0.8Mn (wt%) Super Ferritic Stainless Steel.

X-Ray diffractometer measurements

Figure 1 shows the X-ray diffractogram for the synthesized sample of SFSS taken by using the PANalytical Empyrean X-ray diffractometer with Cu-target (λ = 1.5405 Å) in the angular diffraction range (2θ) between 40° and 100°. Four characteristic reflection intensities with Miller indices corresponding to the diffraction planes of (110), (200), (211), (220) have been observed in the X-ray diffraction pattern. The Miller indices are characterized to have typical of a body centered cubic (*bcc*) space group that consist of all even combinations. It is remarkable that the intensity of the first reflection peak is so much higher than the intensities of the higher angles reflection peaks. These reflections pattern are only belong to α-(Cr,Fe) phase that is the matrix of the SFSS.

To confirm the XRD results, neutron diffraction measurements were carried out and the results presented similar to the SFSS type. Figure 2 shows the neutron diffraction pattern obtained with HRPD-BATAN from the sample of Fe-24Cr-2Si-0.8Mn SFSS synthesized by powder metallurgy. The neutron diffraction pattern confirmed the unit cell of cubic structure for ferrite, α-(Fe,Cr) and no additional diffraction peaks belonging to the secondary phase have been observed, and the lattice parameter was found to be a = 0.28764± 0.00006 nm. Although the intensity of the reflections is sharp and narrow, they stand in stark contrast to the results of the X-ray diffraction presented in Figure 1. There is no significant difference in the intensity between the main reflection plane (110) and other reflection planes at higher angles. These planes show that samples with a single structure of body center cubic (bcc) were successfully synthesized and confirming the high quality of sample preparation and also the refined crystallinity of sample.

Because the interaction of neutrons directly collides with the atomic nuclei, the neutron diffraction technique more accurately measures minor peaks. So that, the neutron diffraction technique revealed, in addition to the ferritic steel profile in Figure 2, some minor peaks that belong to impurities formed in the sample. The minor peaks recently have been identified as a small amount of Al_2O_3 54SiO_2, Al_4C_3, SiC, and $Cr_{23}C_6$ crystals (Parikin et al., 2018).
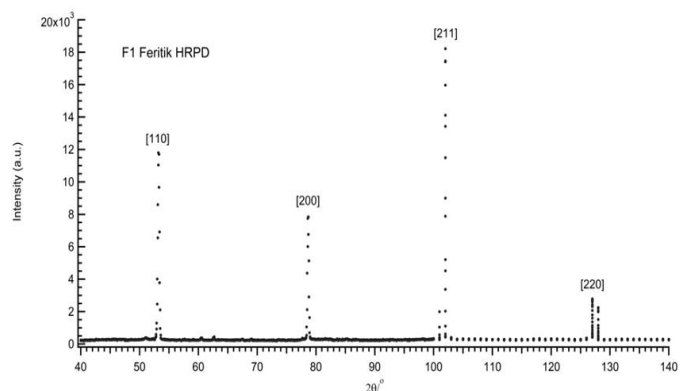
Fig. 2. Neutron diffraction pattern obtained from HRPD-BATAN for Fe-24Cr-2Si-0.8Mn (wt%) SFSS.

50 x magnification	500 x magnification
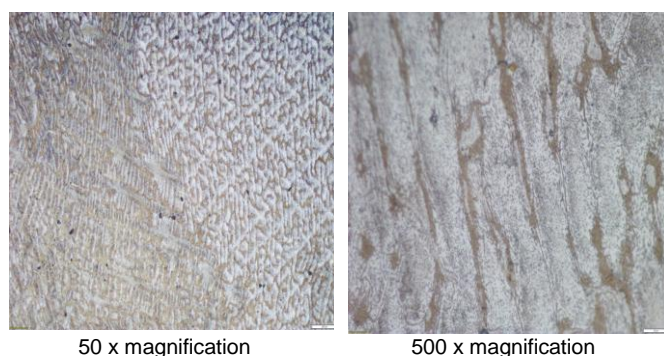
Fig. 3. Optical micrograph of Fe-24Cr-2Si-0.8Mn (wt%) SFSS.

Optical Microscopy and SEM Observations

Optical microscopy

From optical micrographs of the microstructure of SFSS as shown in Figure 3, two different regions can be observed. Although all structures are dominated by α-(Fe,Cr) phases as the matrix of the SFSS and separated by carbide and other intermetallic compound particles, the left region seems to have finer structure as compared to the right region. The XRD and HRPD analysis have investigated both matrices for the SFSS of α-(Fe,Cr) phase to have the same crystal structure, i.e. body center cubic structure. The dendrite arm spacing (DAS) of α-(Fe,Cr) was measured from the optical micrograph about 37.53 ± 8.81

μm. The precipitates segregated in the grain boundary have phases of (Fe,Cr)-carbide and intermetallic compounds (Fe,Cr,C,Si,Ni). Some studies (Carpenteret et al., 2002; Ma et al., 2015; Wieczerzak et al., 2017) have successfully identified this carbide particle as the compound of $(Cr, Fe)_7C_3$. Moreover, mapping the elements shown in Figure 4 provides mainly the chemical composition of particles close to the $(Cr,Fe)_7C_3$. Generally, the grains of α-(Fe, Cr) have dendrite forms, while the shape of $(Cr,Fe)_7C_3$ in the dendrite boundary is rod-like form.
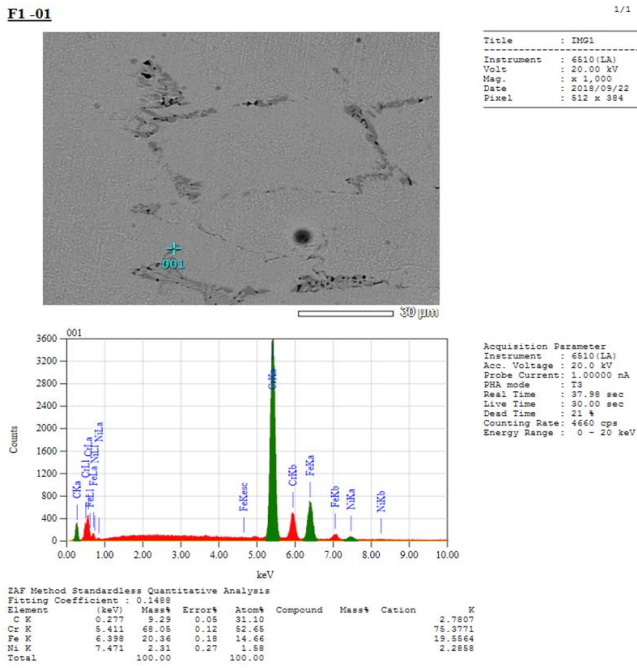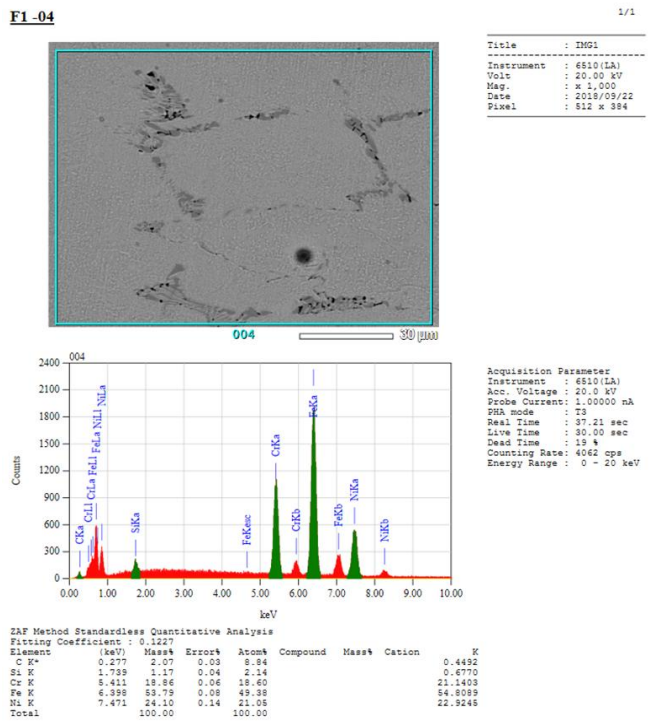
(a)
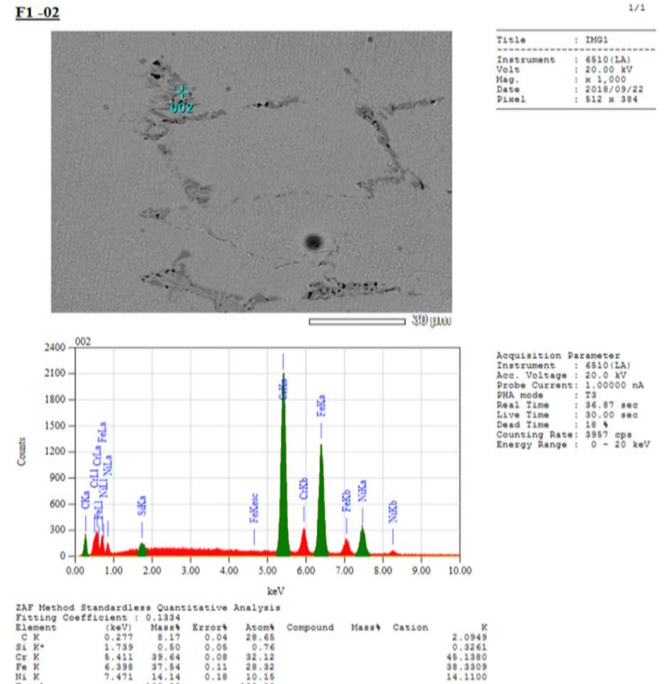
(b)
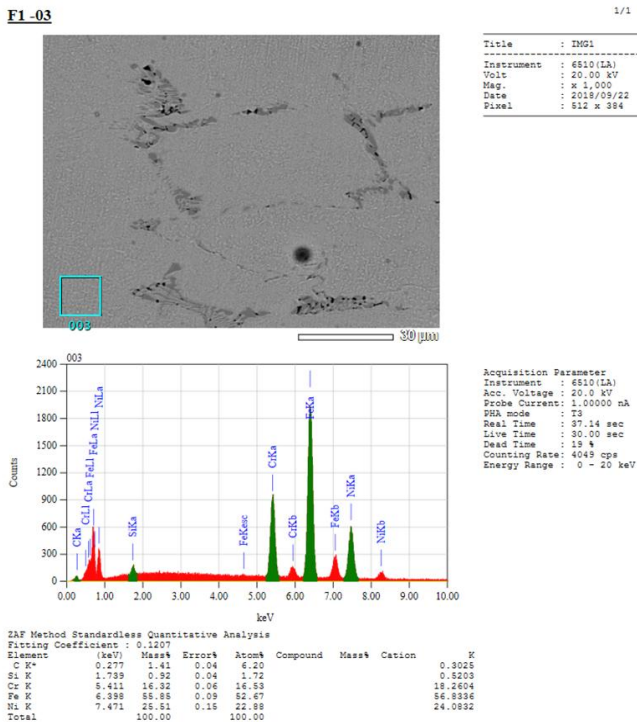
(c)

(d)

**Fig. 4. a-d.** SEM EDS micrographs of the surface of Fe-24Cr-2Si-0.8Mn (wt%) SFSS.

SEM and EDX results

Although C contents in the SFSS alloy is lower than other elements such as Si and Mn, its possibility to react with Cr is higher due to the greater thermodynamic affinity to the Cr (Wieczerzak et al., 2017). Because of that, the intermetallic compound of (Fe,Cr)-carbide might have high possibility to form as precipitates in the interior and grain boundary of the matrix of α-(Fe,Cr). To support the finding of the intermediate phases formation, the EDX elemental analysis were performed on the SFSS sample (see Figure 4a-d). All Cr and Fe contents as compared to C content from the results of identification for the precipitates seen in Figure 4.a have ratio close to 7 and 3. Thus, this precipitate can be $(Cr,Fe)_7C_3$ carbide precipitate. Similar to the precipitate identified in Figure 4.b, ratio of all the metal to C is 7 and 3, which means this has been confirming the precipitate of $(Cr,Fe)_7C_3$ carbide. Interestingly, the free particle zone around the particle of $(Cr,Fe)_7C_3$ carbide seems to have no significant difference of Cr content. Thus, the possibility to form the Cr deflection zone is low in this Fe-24Cr-2Si-0.8Mn SFSS due to the C content in the SFSS lower than 0.05at% as notified in a previous study (Amuda et al., 2016).

STEM, HRTEM and HAADF observations

STEM observation results

STEM bright-field (STEM-BF) image from selected area of the sample shows the morphology of the matrix grains and rod-like precipitate as shown in Figure 5a. The precipitate is about ~400 nm in width and ~2 μm in length. In combination with STEM high-angular dark-field (STEM-HAADF) image and EDX spectrum (as shown in Figure 5 b, c, and d) revealed more detail information of the precipitate. It can be seen clearly, based on contrast variation as well as EDS semi-quantitative analysis that the precipitate contains high Cr. EDX semi-quantification results also show that the precipitate in the ferritic sample approximately consists of 21.21 at%C , 0.62 at%Si, 59.05 at%Cr, 1.02 at%Mn, and 15 at%Fe. The matrix consists of 79.37 at%Fe, 19.33 at%Cr, and 1.29 at%Si, while the elements that were successfully detected at the precipitate about 55.04 at%C, 35.42 at%Cr, and 8.37 at%Fe. The elemental composition of the matrix is close to the previous analysis from the tests performed with Optical Emission Spectrometers such composition is close to the intermetallic compound of $(Cr,Fe)_7C_3$ carbide with high C content as identified in a study of the characterization of cast Fe-Cr-C alloys (Wieczerzak et al., 2015).
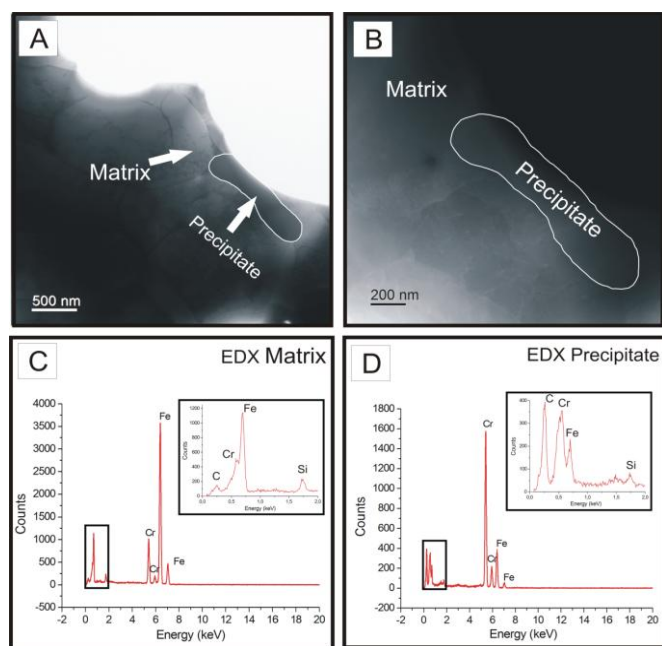
Fig. 5.(a) STEM brightfield image of selected area on the sample showing the morphology of matrix and precipitate (white arrow). (b) STEM-HAADF image together with EDX spectrum of matrix (c) and precipitate (d), respectively.

SAED (Selected Area Electron Diffraction) observation results

Figure 6a shows the TEM bright-field (TEM-BF) image of the matrix together with corresponding selected area electron diffraction (Figure 6b) taken along [001] zone axis of the matrix. SAED analysis, using Diff Tools Digital Micrograph (DM) and JEMS simulation, identified that the matrix has bcc-crystal structure of chromium iron phase in space group Im-3m with the lattice parameters of a = 2.8664 Å (ICSD: 102752). Such result was also obtained by a recent study about solidified Fe-Cr-C alloy (Wieczerzaket al., 2017). TEM bright-field (TEM-BF) image of matrix area and precipitate was presented in figure 6c and corresponds to SAED in figure 6d that shows the additional reflection from the precipitate crystal structure around the SAED of matrix taken along [001] zone axis.
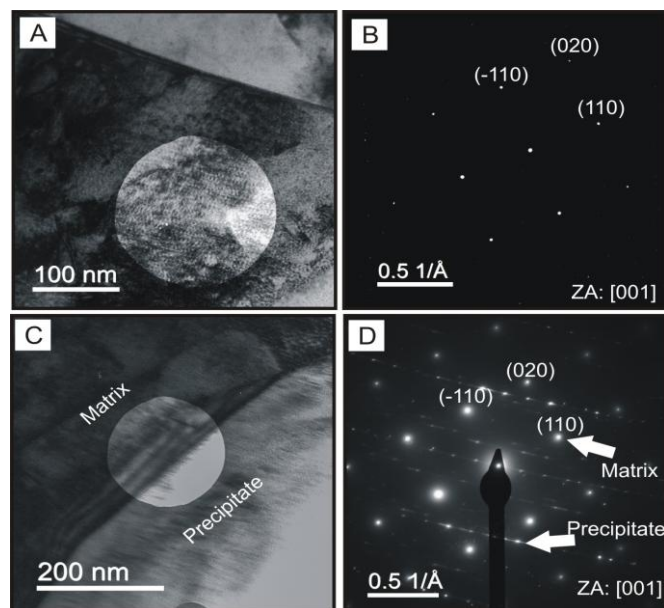
Fig. 6. (a) TEM bright-field (TEM-BF) of the SFSS matrix with (b) selected area electron diffraction (SAED) taken along [001] zone axis. (c) TEM-bright field (TEM-BF) image of area contains interface of matrix-precipitate. Selected area diffraction (d) showed the pattern of matrix along 001 with additional reflections from precipitate.
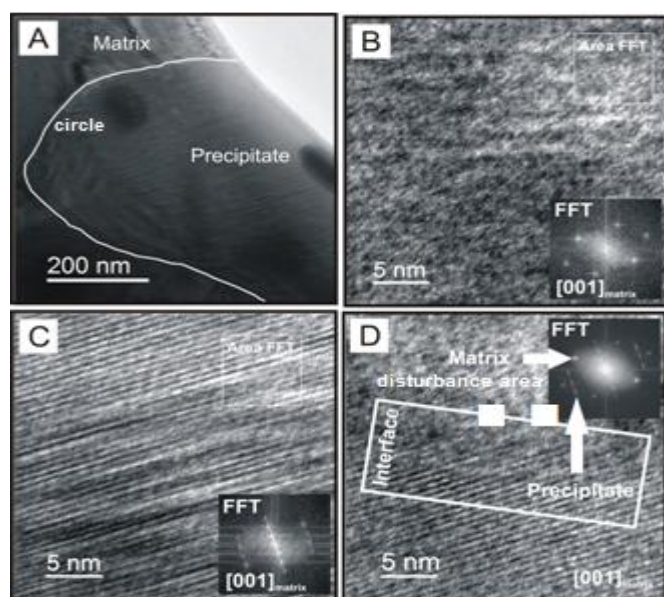
Fig. 7.(a) Energy-filtered TEM (EFTEM) image of the interest area, (b) high-resolution filtered TEM (HRTEM) image of matrix (inset: FFT of HRTEM image of the matrix).(c) HR-Filtered TEM image of precipitate shows strong defects, particulary twinning (d) Filtered (ABSF) HRTEM image of the matrix-precipitate interface show a disturbance area at the interface.

HR-TEM Observation Results

To get more understanding of matrix-precipitates relationship on the same area of STEM (Figure 5) and TEM result (Figure 6), analyses at higher detail were performed by means of high-resolution TEM (HR-TEM) at the same zone-axis of SAED pattern (Figure 7).

Energy-filtered TEM (EFTEM) and high-resolution images are presented in Figure 7. Other form of precipitates, circle with the diameter of 90 nm, formed on the matrix as shown in Figure 7.a. At higher magnification, it can be seen that one of the precipitates formed on the matrix, showed by a brighter area, is probably carbon rich precipitate due to less contrast. Further detail of the precipitates can be seen in Figure 7.c. In this HRTEM image, the precipitate contains a strong lattice defects, such as twinning, which confirmed by FFT image. At the matrix-precipitates interface, as shown in Figure 7.d, one can see unclear part that revealed the presence of local defect on this area. This condition can be induced strong defects from the precipitates.

DISCUSSION

Although the Si content reaches around 2%, the microstructure of SFSS still consists of matrix of $\alpha-$(Cr, Fe) dendrites that have diameter space arm about 37.5 μm and inter-dendrites that contain $(Cr, Fe)_7C_3$ precipitates. The diameter of Si atom which is close to the size of Fe atom will be dissolved in α-(Cr, Fe) as a substitution solution. Since the Si solubility limit in α- (Cr, Fe) is about 3.0% (Yamamoto et al., 2014) the Si content in the interior dendrite detected by an Optical Emission Spectrometer can reach around 2.14%. By contrast, the Cr content in the area around the particles is around 16.59% and this is about 2.01% below the Cr content in the matrix which can reach 18.60%. In addition, the matrix that has body-centered structure has low C content as compare to face center cubic structure (Amuda et al., 2016). Thus, it is estimated that $(Cr,Fe)_7C_3$ precipitate will be dominantly formed in the inter-dendrites. The $(Cr, Fe)_7C_3$ precipitates are formed because of the affinity of C atoms to Cr and Fe both in the matrix and inter-dendrites greater than other atoms such as Si and Mn.

The C content in the stainless steel has been a concern for many previous studies. Atom C can accumulate between dendrites so that carbide precipitation with high C content such as $(Cr,Fe)_{23}C_6$ or $(Cr, Fe)_7C_3$ develops in large, continuous and large sizes. If carbide particles with high C content exist, the possibility of a deficiency of Cr atoms will increase around these particles so that there will be a deflection of the Cr atom or the area known as the Cr deflection zone. As consequent, the creep and corrosion resistances of the stainless steel will decrease at high temperatures in addition to low strength. However, in this study, the C content in SFSS is about 0.25–0.05 %wt. This C content is relatively similar from the range reported by a previous study (0.02– 0.05 %wt) to be able to develop into large carbide particles (Amuda, 2016). Thus, the possibility of decreasing the above properties becomes lower due to not possible to form particles of $(Cr, Fe)_{23}C_6$ carbide with large particle size and Cr deflection zone. Therefore, the microstructure including carbide particles for SFSS produced from this casting is estimated to be quite good for cast component products.

The matrix of SFSS is composed of α-(Cr, Fe) dendrites and the $(Cr, Fe)_7C_3$ precipitates in inter-dendrites. However, the content of C in the $(Cr, Fe)_7C_3$ is quite high. With the different crystal structures, namely the body center cubic for the matrix and hexagonal for the precipitation, through HRTEM and SAED images, it is still difficult to determine orientation relationships despite some previous studies (Gingeli et al., 1997: Guo et al., 2013; Karantzalis et al., 2009; Wiengmoon et al., 2011) have succeeded in determining orientation relations in planes of $(1-100)M_7C_3 // (110)\alpha$ and $(1120) M_7C_3 //(100)\alpha$.

Thus, the coherency between matrix and precipitates in the SFSS is difficult to find out. HRTEM, with its capability, can display smooth surface microstructures to the atomic level so that the orientation of the grain can be distinguished from one another, while XRD and HRPD can identify matrix crystal structures and precipitate via its lattice parameter. Moreover, the structure $(Cr, Fe)_7C_3$ has a characteristic structure in the presence of twin grains as well as observed in previous researchers (Ma et al., 2015). Also, the stacking fault is clearly seen on

the precipitates. Those complex structures lead the precipitates to have high hardness, reaching about 1680 HV0.3 (Yamamoto et al., 2014). Moreover, the precipitates at the inter-dendrite can provide the better inter-dendrite strengthening (Shao et al., 2018). The complexity of the constituent structure is estimated to have low energy for the diffusion process during heat treatment so that the nucleation and precipitate growth process is easy to be occurred.

CONCLUSION

In this present work, we have successfully synthesized a new type of Super Ferritic Stainless Steel (SFSS) via the powder metallurgy method. Detailed and constructive analysis by means several combination techniques revealed that the composition of SFSS was close to Fe-24Cr-2Si-0.8Mn (wt%). Further investigation revealed the presence of precipitates which mostly identified as $(Cr,Fe)_7C_3$ carbides. These detected precipitates are mainly formed inside the dendrites of matrix and the dendrite boundary. This existence of precipitates at the dendrite boundary does not make Cr deflection zone so it is believe that the presence of precipitates will improve the mechanical properties of this new SFSS.

ACKNOWLEDGEMENT

REFERENCES

Amuda, M. O. H., Akintabi, E., Mridha, S., (2016), *Ferritic stainless steel: Metallurgy, application and weldability*, Materials Science and Materials Engineering, Elsevier.

Bella, A. M. T., Henderson, C. M. B., (2016). Rietveld refinement of the crystal structures of Rb2XSi5O12 (X=Ni, Mn). *Crystallographic Communications*, 72, pp.249–252.

Burnett, T. L., Kelley, R., Winiarski, B., Contreras, L., Daly, M., Gholinia,, A., Burke, M.G., Withers, P.J., (2016), Large volume serial section tomography by Xe plasma FIB dual beam microscopy. *Ultramicroscopy*, 161, pp.119–129.

Carpenter, S. D., Carpenter, D., (2003), X-ray diffraction study of M7C3 carbide within a high chromium white iron, *Materials Letters,* 57, pp.4456-4459.

Dani, M., Parikin, Iskandar, R., Dimyati, A. (2017). Investigation on precipitations and defects of the Fe-24Cr-2Si-0.8Mn ferritic super alloy steel. *Indonesian Materials Science Journals* (Jurnal Sains Materi Indonesia), 18(4), pp.173–178.

Dani, M., Untoro P., Putra T. Y. S. P., Parikin, Mayer, J., Dimyati, A., (2015). Transmission electron microscopy characterization of high-temperature oxidation of Fe-20Cr-5Al alloy prepared by focused ion beam technique. *Makara Journal of Technology*, 19(2), pp.85–89.

David, S. A. , Siefert, J. A., Feng, Z., (2013). Welding and weldability of candidate ferritic alloys for future advanced ultra supercritical fossil power plants. *Science and Technology of Welding and Joining*, 18(8), pp. 631–651.

Effendi, N., Darwinto, T., Ismoyo, A. H., Parikin, (2014). 24-chromium ferritic steel magnetic properties. *Indonesian Materials Science Journals* (Jurnal Sains Materi Indonesia), 15(4), pp.187–191.

Effendi, N., Jahja, A. K., Bandriana, Adi, W. A. (2012). Some data of second sequence non standard austentic Ingot A2. *Urania, Scientific Journal of Nuclear Fuel Cycle*, 18(1), pp.48–58

Frølich, S., Leemreize, H., Jakus, A., Xiao, X., Shah, R., Birkedal, H., Almer, J. D., Stock, S. R. (2016). Diffraction tomography and rietveld refinement of a hydroxyapatite bone phantom. *Journal of Applied Crystallography*, 49(1), pp.103–109

Gingeli, A. D. B., Bhadeshia, H. K. D. H., Jones, D. G., Mawella, K. J. A.

(1997). Carbide precipitation in some secondary hardened steel, *Journal of Materials Science*, 32, pp.4815-4820.

Guo, J., Lui, L. G., Li, Q., Sun, Y. L., Gao, Y. K., Ren, X. J., Yang, Q. X. (2013). Characterization on carbide of a novel steel for cold work roll during solidification process, *Materials Characterization*, 79, pp.100-109.

Harjo, S., Kawasaki, T., Gong, W., Aizawa, K. (2016). Dislocation characteristics in lath martensitic steel by neutron diffraction. *Journal of Physics: Conference Series,* 746, pp.1–7.

Humphreys, C. J. (2013). The significance of Bragg's Law in electron diffraction and microscopy, and Bragg's Second Law. *Foundations of Crystallography, Acta Crystallography*, A(69), pp.45–50.

Karantzalis, A.K., Lekatou, A., Mavros, H., (2009, Effect of destabilization heat treatment on the microstructure of high chromium cast iron: A microscopy examination approch, *Journal of Materials Engineering Performance*, 18, pp.1078-1085.

Ma, S., Xing, J., He, Y., Li, Y., Huang, Z., Lui, G., Geng., Q. (2015). Microstructure and crystallography of M7C3 carbide in chromium cast iron, *Materials Chemistry and Physics*, 161, pp.65-73.

Mitchell, D. R. G. (2008). Difftools: Electron diffraction software tools for digital micrograph, *Microscopy Research and Technique*, 71(8), pp.588-593.

OroginLab. (1999). [Software]. Northampton, M. A., USA.

Parikin, P., Dani, M., Jahja, A. K., Iskandar, R., Mayer, J. (2018). Crystal structure investigation of ferritic 73Fe 24Cr 2Si0.8Mn0.1Ni steel for multi purpose structural material applications. *International Journal of Technology University of Indonesia,* 9 (1), pp.78-88.

Shao, Y., Liu, C., Yue, T., Liu, Y., Yan, Z., and Li, H. (2018). Effect of static recrystallization and precipitation on mechanical properties of 00Cr12 ferritic stainless steel, *Metallurgical and Materials Transaction B*, 49(4), pp.1560-1567.

Stadelmann, P. (2012). *Electron Microscopy Software Java Version*, JEMS, ver. 3.3425U2012, CIME-EPFL, Lausanne, Switzerland.

Wieczerzak, K., Bala, P., Dzuirka, R., Tokarski, T., Cios, G, Koziel, T., Gondek, L., (2017), The effect of temperatur on the evolution of eutectic carbide and M7C3 → M23C6 carbide reaction in the rapidly solidified Fe-Cr-C alloy, *Journal of Alloys and Compounds*, 658, pp.673-684.

Wieczerzak, K., Bala, P., Stepien, M., Cios, G, Koziel, T. (2015). Characterization of cast Fe-Cr-C alloy, *Archieves of Metallurgy and Materials*, 60(2), pp.779-782.

Wiengmoon, A., Pearce, J. T. H., Chairuangsri, T. (2011). Relationship between microstructure, hardness and corrosion resistance in 20 wt%Cr, 27 wt%Cr, and 36 wt%Cr high chromium cast iron, *Materials Chemistry and Physics*, 124, pp.739-748.

Yamamoto, K., Inthidech, S., Sasaguri, N., and Matsubara, Y. (2014). Influence of Mo and W on high temperature hardness of M7C3 carbide in high chromium white cast iron, *Materials Transactions*, 55(4), pp.684-689.